Detailed spectroscopy of the Cs_{2} a^{3}Σ_{u}^{+} state and implications for measurements sensitive to variation of the electron-proton mass ratio

S. Sainis, J. Sage, E. Tiesinga, S. Kotochigova, T. Bergeman, and D. DeMille

Phys. Rev. A **86**, 022513 — Published 21 August 2012

DOI: 10.1103/PhysRevA.86.022513

Detailed Spectroscopy of the Cs_2 $a^3\Sigma_u^+$ State and Implications for Measurements Sensitive to Variation of the Electron/Proton Mass Ratio

S. Sainis and J. Sage
Department of Physics, P. O. Box 208120, Yale University, New Haven, Connecticut 06520

E. Tiesinga
National Institute of Standards and Technology, 100 Bureau Drive, Stop 8423, Gaithersburg, Maryland 20899, USA

S. Kotochigova
Physics Department, Temple University, Philadelphia, PA 19122

T. Bergeman
Department of Physics and Astronomy, SUNY, Stony Brook, NY 11794-3800

D. DeMille
Department of Physics, P. O. Box 208120, Yale University, New Haven, Connecticut 06520

We present spectroscopic data on moderately bound levels in the Cs_2 $a^3\Sigma_u^+$ state. The data have sufficient resolution to be sensitive to rotational and second-order spin-orbit splittings as well as hyperfine and vibrational structure. Quantum numbers are assigned to the levels via selection rules and a global fit to other available data for the $a^3\Sigma_u^+$ and coupled $X^1\Sigma_g^+$ states. The analysis focuses in particular on nearly degenerate pairs of a and X state levels, energy differences between which can be highly sensitive to possible variations in the electron-to-proton mass ratio (cf. DeMille *et al.*, Phys. Rev. Lett. **100**, 043202 (2008)). We also characterize the electric (E1) and magnetic (M1) dipole transition strengths between nearly degenerate a and X ro-vibrational levels and find that both types of transitions are feasible with current technology and could give complementary information.

PACS numbers: 06.20.Jr,33.15.Pw,33.20.Wr,42.62.FI

I. INTRODUCTION

Several recent papers [1, 2] have pointed out the possibility to use measurements of molecular energy splittings as a sensitive probe for possible variations in the electron-to-proton mass ratio, $\mu \equiv m_e/m_p$. The essential point of these proposals is that molecular electronic potentials are determined primarily by electrostatics, and hence depend parametrically on the Rydberg energy, $\mathcal{R}$ (independent of the proton mass m_p); while molecular vibrational and rotational energies depend on the molecular reduced mass, which is dominated by the mass of the contituent nuclei and hence is proportional to m_p. For example, molecular vibrational frequencies scale parametrically as $\mathcal{R}\sqrt{\mu}$. Therefore, if μ were to vary, the energy of a molecular vibrational state would change relative to the potential well itself. Moreover, the size of this variation can grow as the vibrational quantum number increases within a single molecular potential (up to a maximum given by roughly 3/4 of the dissociation energy [1]).

In [1] a potentially advantageous situation is discussed, which uses the existence of more than one molecular electronic potential to amplify the sensitivity to variations in μ. In particular, here the strategy is to find pairs of closely-spaced molecular levels: one associated with a high-lying vibrational state of the ground-state electronic potential, and the other associated with a low vibrational state of an excited potential (associated with a long-lived electronic state). As discussed in detail in [1], measurements of the energy splitting between such a pair can provide both a high absolute sensitivity to variations in μ (from the high-lying vibrational level) and good relative insensitivity to experimental errors (due to the small transition frequency between the levels). Bialkali molecules were pointed out as an example of this behavior, since in these species there exists a relatively deeply bound absolute ground state (the $X^1\Sigma_g^+$ state) that overlaps with a shallow excited state potential (the $a^3\Sigma_u^+$ state) that converges to the same atomic asymptote. Such molecules also seem particularly attractive for this application, since it has been demonstrated that they can be produced at ultracold temperatures, allowing narrow linewidths and hence excellent sensitivity to energy shifts. In [1], the specific case of Cs_2 was discussed and one example of a near-degeneracy of the desired type was presented.

Here we present spectroscopic data (described in more detail in [3]) that provides precision information on several levels of the Cs_2 a state, as well as on the relative position of nearby levels of the X state. We also present a global fit to most available spectroscopic data on the Cs_2 a state, which yields a potential curve suitable for use in predicting possible $a - X$ near-degeneracies that have not yet been observed. We also predict electric and magnetic dipole transition strengths between a and X state

sublevels that could be useful for precise measurements of their splitting.

Our analysis of vibrational, rotational, hyperfine and second-order spin-orbit structure in the Cs_2 $a^3\Sigma_u^+$ state may be compared with previous studies of the analogous state in Na_2 [4, 5], NaRb [6], NaCs [7], LiCs [8], KRb [9] and Rb_2 [10]. Some of these studies used Fourier transform spectroscopy from chosen excited states to access a wide range of a state levels, with resolution typically 0.03 cm^{-1}. Other methods, as described in [4, 5, 10] were able to achieve line uncertainties as small as 15 MHz, and thus obtained more detailed information on the hyperfine structure.

The observations analyzed here come from two sources. The first is the data set reported here, from 6 vibrational levels (v = 28 - 31, 37, 38) extending over binding energies E_b between -50 cm^{-1} and -14 cm^{-1}. We measured 22 energy level differences to 30 MHz, and 6 absolute binding energies to 340 MHz to 420 MHz (one standard deviation combined statistical and systematic uncertainties are given). The second source is information on the Cs_2 $a^3\Sigma_u^+$ state from the work of Li, Xie *et al.* [11, 12] who obtained data on 1440 rovibrational levels observed by emission from an electronically excited triplet state. Although hyperfine structure was not resolved, these observations did yield much improved values for the a state dissociation energy and equilibrium internuclear distance, R_e.

Other data in the literature that is relevant to the Cs_2 $a^3\Sigma_u^+$ state, but which is not included in the present analysis, include data on Feshbach resonances observed by [13–15] and subject to careful analysis by [16, 17], yielding information on the hyperfine structure of weakly bound levels. Also, [18] reported data on more than 100 hyperfine-rotation levels with uncertainties of 12 MHz to 24 MHz, extending down to 2.5 cm^{-1} below the lowest ($f_a + f_b = 3+3$) atomic hyperfine limit. In the future, we hope to include these data together with the present data set in a combined analysis. However, there are numerical complications with a more comprehensive analysis.

Because our analysis incorporates hyperfine-mediated couplings between nearly degenerate a and X state levels, we also summarize the Cs_2 X state spectroscopic data. There exist a series of progressively more extensive observations of this state, culminating in the observations of Amiot and Dulieu [19]. From this reference an RKR (Rydberg-Klein-Rees [20]) potential curve for the X state is available that extends up to about 50 cm^{-1} below the dissociation limit. The long range potential terms (dispersion and exchange terms) were also estimated by [19] and further refined by [18]. Weickenmeier *et al.* [22] observed splittings of X state levels with vibrational quantum number, v=130 to 137 and rotational quantum number, J=17 to 55, induced by coupling with the a state. Another piece of useful information is the precise determination of the dissociation limit of the Cs_2 $X^1\Sigma_g^+$ state by Danzl *et al.* [23]. There has been a careful reanalysis of the X state potential by [24] using a direct fit to analytic potential forms, and this achieved a more exact fit to the data of [19]. However, because in the present work we are modeling both X and a state data, we prefer to introduce an exchange potential explicitly, which is not easily achieved with these analytic forms. Our potential forms are discussed in Sec. III. For the X state, we retain the IPA (Inverted Perturbation Approach [21]) potential of [19], which is an extension and refinement of the RKR potential, and make only slight adjustments in the long range potential parameters of [18] to be compatible with the improved dissociation limit of [23].

To a first approximation, the experimental observations reported here are consistent with a simple model of hyperfine structure (hfs) with no singlet-triplet mixing and no second-order spin-orbit terms. Our more detailed analysis shows that singlet-triplet mixing by hyperfine effects and also second-order spin-orbit terms are needed to model the data accurately. For a presentation of extensive precision measurements of hyperfine effects in a molecular $^3\Sigma_u^+$ state other than an alkali dimer, see, for example, work on the N_2 $a^3\Sigma_u^+$ metastable state in [25, 26].

Below, we first describe the experimental methods and results (section II), then develop the theoretical model in several steps and apply it to the data (sections III-V). In section VI we present some implications of our results for performing measurements sensitive to the electron/proton mass ratio.

II. EXPERIMENTAL METHOD

We experimentally locate deeply bound $a^3\Sigma_u^+$ levels using two-color photoassociation (PA) spectroscopy [18, 27]. The basic approach is shown in Figure 1. A continuous-wave (cw) photoassociation (PA) laser resonantly excites pairs of ultracold Cs atoms into a bound state of the short-lived Cs_2 $0_g^-(6P_{3/2})$ potential (dissociating to the $6^2S_{1/2} + 6^2P_{3/2}$ asymptote) [28]. This state decays to a manifold of metastable $a^3\Sigma_u^+$ vibrational levels, which are ionized by a pulsed laser after a period of PA. A tunable cw probe laser also is applied, at the same time as the PA laser, to search for resonances between the desired $a^3\Sigma_u^+$ levels and the $0_g^-(6P_{3/2})$ level excited by the PA laser. On resonance, the probe laser causes an Autler-Townes splitting which (if the coupling is sufficiently strong) effectively shifts the excited state out of resonance with the PA laser, and thereby decreases the rate of molecule formation. Hence we scan the probe laser frequency and look for resonant depletion of the ion signal. Use of PA levels in the pure long-range well of the $0_g^-(6P_{3/2})$ state enables access to deeply bound $a^3\Sigma_u^+$ levels, because of favorable Franck-Condon factors [29, 30].

Ultracold Cs atoms are collected in a forced dark-spot magneto-optical trap (MOT) [31, 32]. Under typical conditions, the Cs atom density n, atom number N, and temperature T are $n \approx 4 \times 10^{11} cm^{-3}$, $N \approx 2 \times 10^8$, and

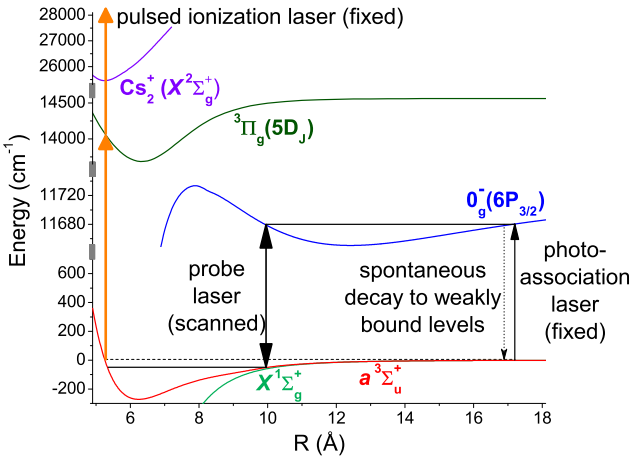

FIG. 1: (In color online.) The relevant potential energy curves of Cs_2 and an overview of the optical transitions used in the experiment.

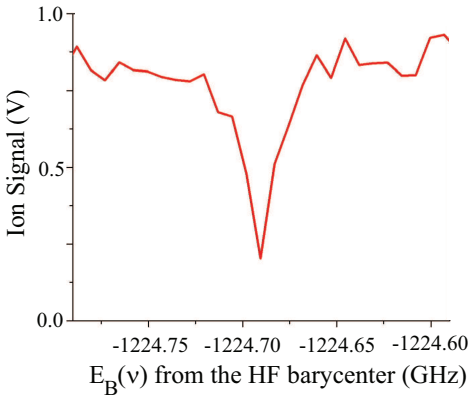

FIG. 2: (In color online.) Typical plot of ion signal vs. probe laser frequency. Shown here is a scan over the rotation-hyperfine "anchor line" for v=30, with nominal quantum numbers $f = 8, \ell = 0, F = 8$, at binding energy $E_b = -1224.670$ GHz.

$T \approx 100\ \mu$K - 200 μK. After a period of collection in the MOT, the Cs atoms are released and optically pumped into the $6^2S_{1/2}\ f = m_f = 4$ "spin-stretched" state. This spin-polarization is crucial to our experiments. Since the $Cs_2\ 0_g^-(6P_{3/2})$ state has unresolved hyperfine structure, PA of unpolarized atoms in the MOT leads to excitation of an incoherent mixture of many degenerate nuclear spin orientations. Because the hyperfine structure *is* fully resolved in the $Cs_2\ a^3\Sigma_u^+$ state, even when the probe laser is tuned to a given bound-bound resonance, only a small fraction of the molecular population can be affected by the probe. Due to the significant shot-to-shot noise in ionization signals, such small fractional depletion signals prove very difficult to observe. By contrast, using a nuclear spin-polarized sample enables us to find probe transitions that couple to the entire excited-state population and hence lead to observably large depletion signals.

The time sequence of the experiment is as follows. After loading the dark SPOT MOT for ≈96 ms, the trapping laser beams are turned off at time $t = 0$. At the same time, a "fill-in" laser beam tuned to the atomic $6^2S_{1/2}\ f = 3 \rightarrow 6^2P_{3/2}\ f' = 4$ frequency is turned on, in order to pump all population into the $f = 4$ state from the dark $f = 3$ state (where most atoms reside in the dark SPOT MOT). Simultaneously, the magnetic field gradient of the MOT is switched off, and replaced with a uniform B-field that gradually builds up to a value B ≈0.4 mT (where 0.1 mT = 1 G) along the z-axis, reaching its final value within ≈ 1 ms. At $t = 1$ ms, an additional "polarizing" laser beam, σ^+ polarized and tuned to the $6^2S_{1/2}\ f = 4 \rightarrow 6^2P_{3/2}\ f' = 4$ transition, is switched on. The fill-in and polarizing beams serve to prepare the Cs atoms in the $f = 4, m_f = 4$ state. The PA and probe lasers, each directed along the z-axis and circularly polarized, are turned on at $t = 1.5$ ms and stay on until $t = 4$ ms. Then, at $t = 4.1$ ms, the ionizing laser pulse is applied. The entire sequence repeats at 10 Hz repetition rate.

The external cavity diode laser used for PA is frequency-stabilized by locking to a confocal Fabry-Perot interferometer (FPI), which is in turn locked to a MOT laser. The probe laser is a tunable Ti:Sapphire laser, whose beam is spatially overlapped with the PA laser and the Cs atom cloud in the MOT; the probe has intensity $I_{probe} \approx 10\text{W/cm}^2$ at the interaction region. A pulsed dye laser generates the light for photoionization of the Cs_2 molecules formed after decay of the PA state. The ionization scheme [33] uses pulses with duration ≈ 5 ns and energy ≈ 15 mJ at wavelength ≈ 716 nm to simultanously ionize a wide range of high-lying vibrational levels of the $a^3\Sigma_u^+$ state formed via PA. The resulting Cs_2^+ ions are mass-selectively detected via their time of arrival on a channeltron ion multiplier. At each probe laser frequency the data is typically averaged over 10 preparation/detection sequences. The probe laser is stepped by 7.5 MHz. Sensitivity to depletion in the ion signal, resulting from the probe laser, is optimal when the channeltron gain is adjusted to ensure it operates in a linear regime (i.e., the output is not saturated). We confirm detector linearity by reproducing the two-color PA spectra of [18, 34, 35], using the $1_u\ (6^2S_{1/2} + 6^2P_{3/2})$ state of Cs_2 as the intermediate resonance. We also confirm the spin-polarization of the atoms by reproducing the PA spectra from polarized atoms observed in [36]. Figure 2 shows a typical ion depletion signal as the probe laser is tuned through a resonance. Other experimental data scans are shown in Figure 8.

Initial state identification and approximate quantum numbers are assigned to each $a^3\Sigma_u^+$ level, according to the following logic. To first approximation, moderately bound levels of the $a^3\Sigma_u^+$ state can be described as eigenstates in the $e_{SI,f}$ basis $|[(S, I)f, \ell], FM_F\rangle$, where $\mathbf{I}$ is the total spin of the pair of Cs nuclei; $\mathbf{S}$ is the total electron

spin; $\mathbf{f} \equiv \mathbf{S} + \mathbf{I}$; $\boldsymbol{\ell}$ is the rotational angular momentum; $\mathbf{F} \equiv \mathbf{f} + \boldsymbol{\ell}$; and M_F is the projection of $\mathbf{F}$. In our notation, the parentheses in $(S, I)f$ indicate that $\mathbf{S}$ and $\mathbf{I}$ are coupled to form $\mathbf{f}$, while the brackets indicate that $\mathbf{f}$ and ℓ are coupled to form $\mathbf{F}$. For pure $a^3\Sigma_u^+$ states, $S = 1$ and the hfs interaction dominates the sublevel structure within a given vibrational level, splitting levels with different f according to $E_{hf} = \frac{A_{hf}}{4}[f(f+1) - S(S+1) - I(I+1)]$, where $A_{hf} = 2.29567$ GHz is the atomic Cs $6s_{1/2}$ hfs constant [39]. For each value of f, there is a manifold of closely-spaced rotational states with energy $B_v \ell(\ell+1)$, where $B_v \approx 0.1$ GHz. Finally, the degeneracy between states with the same ℓ and f, but different F, is lifted by a 2$^{\text{nd}}$-order spin-orbit (SO2) interaction whose effect on the states studied here is somewhat smaller than the rotational energy [40]. In the present discussion, the notation $\mathbf{f} \equiv \mathbf{I} + \mathbf{S}$ applies to atomic states as well as the molecular states.

The difference between the frequencies of the resonant probe and PA lasers yields the binding energy for the $a^3\Sigma_u^+$ level, relative to the initial state of two free Cs atoms in the $6^2S_{1/2}, f = 4$ level. For convenience, we report the binding energy E_b relative to the hfs barycenter, located 8.04 GHz below the $6^2S_{1/2}\ f=4 + 6^2S_{1/2}\ f=4$ asymptote. The absolute PA laser frequency is known since it is tuned to rotational levels of the Cs_2 $0_g^-(6P_{3/2})$ state whose energies were measured previously [28]. The actual observed $0_g^-(6P_{3/2})$ energy level positions (previously unpublished, but communicated to us by N. Bouloufa and O. Dulieu), as well as the most recent potential for the $0_g^-(6P_{3/2})$ state from [37] are given in the Supplementary data file [38]. The positions of these levels are independently confirmed in our lab, at lower accuracy, using a commerical wavemeter. The probe laser frequency on resonance is determined for a few lines with this wavemeter, but usually (more accurately) as follows. Within each observed vibrational level in the $a^3\Sigma_u^+$ state, one strong probe resonance is designated as the "anchor" line. (This is the line corresponding to the least-bound of the ℓ=0 sublevels of the vibrational state observed with σ^+-polarized probe light, which is assigned to the $f = 8, \ell = 0, F = 8$ hyperfine/rotational sublevel of the $a^3\Sigma_u^+$ state.) The probe laser frequency at the anchor line is first determined crudely with the wavemeter. Based on this determination a known, nearby one-photon PA resonance is found and chosen to act as a frequency reference. The probe laser is tuned from this reference line to the anchor line, while monitoring its transmission through a scanning confocal Fabry-Perot interferometer (FPI) with 1 GHz free spectral range (FSR). By measuring the (non-integer) number of FSRs traversed, the position of the anchor line with respect to the reference line (referred to as "FPI offset") is determined. Finally, the positions of other hyperfine/rotational sublevels within the same vibrational state are determined, relative to the anchor line, by the same method.

Uncertainties in the level positions are evaluated as follows. The excited state energies used for the PA and reference lines are known to 150 MHz −300 MHz from Ref.[28], while the absolute uncertainty in our wavemeter is 600 MHz. Errors in the FPI offset are much smaller than both of these, so the uncertainty in binding energy E_b is the quadrature sum of the uncertainties in the PA and reference (or directly measured probe) lines. For a few cases, the energy of a $a^3\Sigma_u^+$ level is measured using two different intermediate PA levels (and the two correspondingly different probe frequencies). The energy determined by both routes is consistent within the uncertainties. Uncertainties in the relative energy of rotational/hyperfine sublevels within a vibrational level, determined by the FPI offset method, are much smaller. They are dominated by the uncertainty in locating the peak position of each line, which–due to limited signal-to-noise–we take as the half width at half maximum of the line, which is typically ≈ 20 MHz. Additional errors due e.g. to uncertainty in the FPI FSR, nonlinearity in the FPI or probe laser tuning mechanism, etc. are estimated to be negligible. Zeeman levels shifts due to the 0.4 mT (=4 G) bias field are also negligible, and henceforth we ignore Zeeman shifts unless explicitly stated otherwise.

In our experiment we start with ultracold pairs of spin-polarized Cs atoms. Consequently, the initial state of the pair has $f = m_f = 8$, and only pairs with $\ell = 0$ are excited by the PA laser. Hence, initially $F = M_F = 8$. Vibrational levels of the Hund's case (c) $0_g^-(6P_{3/2})$ state have resolved rotational levels J', where $\mathbf{J'} = \boldsymbol{\ell'} + \mathbf{S'} + \mathbf{L'}$, $L' = 1$ is the electron orbital angular momentum, and $S' = 1$. The PA laser is tuned to excite $J' = 2$ levels, which are a mixture of $\ell' = 0, 2$, and 4 [41]. The PA laser is σ^+ polarized, so electric dipole (E1) selection rules ensure $F' = M'_F = 9$. Since $\mathbf{F'} = \mathbf{J'} + \mathbf{I'}$ and $F' = 9$, only $I' = 7$ is excited. For the probe laser, either σ^+ or σ^- polarization is used. From E1 selection rules for the probe transition, it follows that only $a^3\Sigma_u^+$ states with $I = 7$, $\ell = 0, 2, 4$, and $F = M_F = 10$ ($F = 8, 9, 10$, $M_F = 8$) are observed with probe polarization σ^- (σ^+). Figure 3 summarizes the approximate quantum numbers and E1 selection rules graphically.

We observe multiple sublevels for several $a^3\Sigma_u^+$ vibrational states v with binding energy $E_b(v)$ in the range −400 GHz to −1500 GHz. The level positions and line strengths qualitatively agree with calculations based on an initial $a^3\Sigma_u^+$ potential constructed from the results of Ref. [18] and the $0_g^-(6P_{3/2})$ potential of Ref. [37]. The predictions of vibrational and rotational energies together with the approximate hyperfine structure discussed above are used to guide an initial assignment of quantum numbers to the observed states. In all we observe 28 energy levels across 6 vibrational states. The data are summarized in Table II. Additional details (e.g. qualitative measures of the line strengths) are given in Ref. [3]. As discussed in Ref. [1] and also in more detail below, one of the most striking features of our data is the appearance of an "extra" line with $F = 10$ in the $v = 37, f = 7$ manifold of states. We attribute this line to the presence of a near degeneracy between a pair of

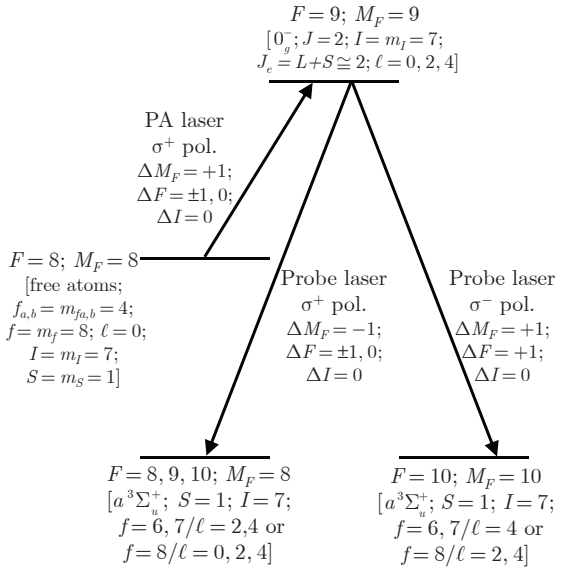

FIG. 3: The approximate quantum numbers of the scattering and molecular states used in the experiment.

$a^3\Sigma_u^+$ and $X^1\Sigma_g^+$ states, and an associated strong mixing between these states.

III. HAMILTONIAN

We now turn to the analysis of the data presented in the previous section. The Hamiltonian for the Cs_2 a and X states may be written

$$H = H_{BO,\eta} + H_{kin} + H_{rot} + H_{hf} + H_{SO2}, \qquad (1)$$

where $H_{BO,\eta}(R)$ includes the Born-Oppenheimer potentials for the two states, $\eta = X^1\Sigma_g^+$ and $a^3\Sigma_u^+$; H_{kin} represents the kinetic energy of vibrational motion in R, the internuclear separation; H_{rot} represents the rotational motion; H_{hf} the hyperfine structure effects; and $H_{SO2}(R)$ the second-order spin orbit or effective spin-spin term. The H_{hf} term has diagonal elements for the a state and off-diagonal elements that can lead to mixing of the a and X states.

The Born-Oppenheimer potentials in $H_{BO,\eta}(R)$ are modeled with three regions, demarcated by R_L and R_R:

$$\begin{aligned} R \le R_L \ &: \quad V_L(\eta,R) = C(\eta) + b(\eta)/R^6; \\ R_L < R < R_R \ &: \quad V_W(\eta,R); \\ R_R \le R \ &: \quad V_R(\eta,R) = V_{\rm disp}(R) + V_{\rm exch}(\eta,R) \end{aligned} \qquad (2)$$

$C(\eta)$ and $b(\eta)$ are adjusted to provide a smooth transition to $V_W(\eta,R)$ at $R=R_L$. For each electronic state, R_L is chosen such that $V_L(\eta,R_L)$ lies adequately above the dissociation energy. R_R was fixed at 12 Å (where 1 Å= 10^{-10}m) for both states, somewhat beyond the Le Roy radius [42] of 10.5 Å.

For the $X^1\Sigma_g^+$ state, $V_W(X^1\Sigma_g^+,R)$ was obtained from the accurate RKR potential given in [19]. For the well region of the a state, we use an expansion of the form [35, 43]:

$$V_W(a^3\Sigma_u^+,R) = T_e + \sum_{i=2}^{I} a_i \left(\frac{R-R_e}{R+bR_e}\right)^i. \qquad (3)$$

Here R_e is the internuclear distance at the minimum of the potential of the electronic state in question. The parameter b is adjusted to achieve an optimum fit with a minimum number of parameters. The coefficients a_i were determined by a fit to the data of [12] combined with the data presented here. The quality of the fit will be discussed below.

The dispersion terms in V_R are given by

$$V_{\rm disp} = -\frac{C_6}{R^6} - \frac{C_8}{R^8} - \frac{C_{10}}{R^{10}} - \frac{C_{12}}{R^{12}}. \qquad (4)$$

The C_N parameters in our fits are those given by [18] with slight adjustments (see below). For the exchange energy, we use the form given in [19]:

$$V_{\rm exch} = \pm A_{\rm exch} R^{\gamma_{\rm exch}}\ e^{-\beta_{\rm exch} R}. \qquad (5)$$

where the $+(-)$ sign applies to the $a(X)$ state. The parameters $A_{\rm exch}$ and $\beta_{\rm exch}$ are adjusted to optimize the fit to the data. At the same time, these parameters and the coefficients a_i in V_W must be such that the transition between V_W and V_R is smooth (in its value and in the derivatives). In light of these conditions and the recent more accurate determination of the dissociation energy of the X state by [23], our optimized dispersion parameters differ slightly from previous values (see Table IV). Figure (4) displays potentials calculated from the above parameters as obtained from the fitting process discussed below.

With regard to these potentials, we emphasize the goals and limitations of this work, which focuses on the energy region sampled by the data obtained in Ref. [3]. The analysis in [24] obtained a comprehensive fit to the X data of [19], superior to the IPA fit in [19] itself. Furthermore, as stated above, Feshbach resonance data [13–15], the analysis of [16, 17] and the data of [18] together with the recent redetermination of $D_e(X)$ [23] provide a more precise characterization of the long range potentials. D_e is the energy interval between the potential minimum and the hyperfine center of gravity of the free atoms. A truly comprehensive fit to Cs_2 X and a state data remains a challenge. Our own attempts with an analytic potential of the Morse Long Range (MLR) form [44] did not yield a difference between the X and a potentials that would converge to zero beyond the Le Roy radius [42], at which the atomic wavefunction overlaps become negligible, and therefore we chose to use an explicit exchange potential.

The rotational energy operator involves the rotational angular momentum operator $\boldsymbol{\ell}$:

$$H_{rot} = \frac{\hbar^2}{2\mu}\frac{\boldsymbol{\ell}^2}{R^2}. \qquad (6)$$

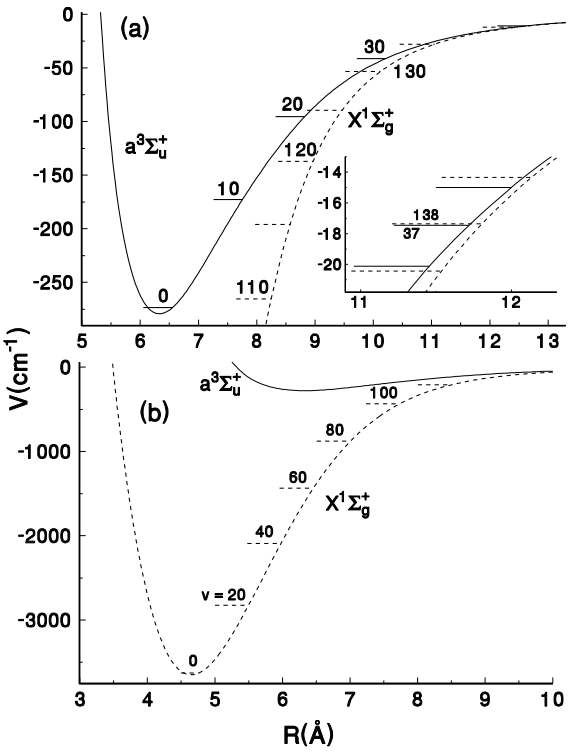

FIG. 4: Potentials for the Cs_2 $X^1\Sigma_g^+$ and $a^3\Sigma_u^+$ states with vibrational numberings. The inset in part (a) shows near-degenerate levels of especial interest in this study.

Vibrational energies come from the operator for kinetic energy along the internuclear axis,

$$H_{kin} = -\frac{\hbar^2}{2\mu}\frac{\partial^2}{\partial R^2}; \tag{7}$$

here, $\mu = M/2$ is the reduced mass, where M is the atomic mass. To evaluate the second derivative, we use the discrete variable representation (DVR), employing a set, R_i, of discrete grid points in R, as described in [45], with a scaling function as in [46]. To obtain maximum accuracy for a given mesh, all N grid points are used to calculate the second derivative, and therefore one has an $N \times N$ Hamiltonian matrix. Rovibrational eigenfunctions, labeled by $|\eta\,\ell, v\rangle$, may be written $|\eta\ell, v\rangle = \sum_i |R_i\rangle\langle R_i|\eta, \ell, v\rangle$. Here the $|R_i\rangle$, each an N-component vector with j^{th} component δ_{ij}, can be considered a basis of position eigenstates, or the set of grid points.

In the approximation that hyperfine and second-order spin-orbit effects are negligible, rovibrational energies $E(\eta, \ell, v)$ and eigenfunctions $|\eta, \ell, v\rangle$ are computed by diagonalizing DVR matrices $H0^{\eta\,\ell}$, with matrix elements $H0^{\eta\,\ell}_{ij} = \langle\eta\,\ell|\langle R_i|H_{BO,\eta} + H_{kin} + H_{rot}|R_j\rangle|\eta\,\ell\rangle$; nonzero off-diagonal elements with $i \neq j$ are produced by the second derivative in H_{kin}. Thus $E(\eta\,\ell, v) = \langle\eta\,\ell, v|H0|\eta\,\ell, v\rangle$. DVR eigenvalues give the rovibrational energies without the use of explicit centrifugal distortion parameters. Where needed, the rotational constant for vibrational level v, $B_v = (\hbar^2/2\mu)\sum_i\langle\eta\,\ell = 0, v|R^{-2}|\eta\,\ell = 0, v\rangle$, can be explicitly calculated via $\langle R_i|R^{-2}|R_j\rangle = \delta_{ij}/R_i^2$.

IV. HYPERFINE STRUCTURE

We discuss hfs effects with four modes or levels of approximation. The first considers atoms at long range, in the atomic limit. Second, we consider a model with no coupling between triplet and singlet molecular states, hence with hfs only in a states. Third, we consider triplet-singlet mixing. Finally, we introduce second-order spin-orbit effects, which couple electron spins to the rotation of the molecule.

We describe the atomic limit in the $e_{fafb,f}$ representation, where f_α is the sum of electron spin $S_\alpha = 1/2$ and nuclear spin $I_\alpha = 7/2$ in Cs atom $\alpha = a, b$. Basis elements in this representation are denoted $|(S_a, I_a)f_a, (S_b, I_b)f_b, f\rangle$, or simply $|(f_a, f_b)f\rangle$, in the molecular frame. The hyperfine Hamiltonian of the pair of separated atoms is

$$H_{hf} = A_{hf}(\mathbf{I}_a \cdot \mathbf{S}_a + \mathbf{I}_b \cdot \mathbf{S}_b). \tag{8}$$

We write the molecular hyperfine energies relative to the molecular hyperfine center-of-gravity, f_{cg}:

$$E_{hf} = 4A_{hf}(f_a + f_b - f_{cg}); \quad f_{cg} = 2I_A + \frac{1}{2I_A + 1} \tag{9}$$

with $f_{cg} = 57/8$ for two Cs atoms with I_A=7/2. The molecular hfs center of gravity lies $(9/2)A_{hf} = 10.33456$ GHz above the $f_a + f_b = 3 + 3$ limit. In these equations, $\mathbf{f}_\alpha = \mathbf{S}_\alpha + \mathbf{I}_\alpha$ $\mathbf{S} = \mathbf{S}_a + \mathbf{S}_b$; $\mathbf{I} = \mathbf{I}_a + \mathbf{I}_b$; $\mathbf{f} = \mathbf{f}_a + \mathbf{f}_b = \mathbf{S} + \mathbf{I}$.

In principle, one can generalize H_{hf} in Eq. 8 to be dependent on the internuclear distance R. At the accuracy of the experimental data here we cannot justify this extension. For the Na_2 [4] and Rb_2 [10] dimers, the $R-$dependence has a small but observable effect.

In the simplest approximation for the molecular hyperfine Hamiltonian, $H_{hf} = (A_{hf}/2)\mathbf{I}\cdot\mathbf{S}$, where $I = 0, 1, ...7$ and S=0 or 1. This interaction is diagonal in the $e_{SI,f}$ basis, with energies as given in Sec. II:

$$E_{hf}(S, I, f) = \frac{A_{hf}}{4}[f(f+1) - S(S+1) - I(I+1)] \tag{10}$$

The allowed values for I and S are limited by the symmetry imposed by bosonic atoms in a homonuclear molecule to $I + S + \ell =$ even. For even ℓ (positive parity), there are three possible combinations of (S, I) for f = 2,4, and 6, as determined by the triangle rule. Table I lists all possible states. Note that for even ℓ, singlet states occur in the Hamiltonian matrices only for f=0,2,4, and 6.

Figures 5a and 6a, for the v=37 and v=38 vibrational levels, respectively, show energy levels with this representation as a function of $\ell + f/10$. The calculated energies are obtained from a fit to the experimental data with a function $E = G(v) + B(v) + (A_{hf}/2)\mathbf{I}\cdot\mathbf{S}$. Since data on singlet states is not available in this region and since this simplest molecular hfs model includes no singlet-triplet coupling, nearby singlet states are omitted in these plots, but are shown in Figs. 5b and 6b. The abscissa variable is chosen to present the hfs as clearly as possible. Hyperfine levels for a given ℓ are grouped together, since $f \leq 8$, $f/10 < 1$. For each ℓ, the hyperfine levels for the $^3\Sigma_u^+$ state have three branches that separate from each other linearly with f, proportional to A_{hf}.

Since H_{BO}, H_{kin}, and H_{rot} are all diagonal in S, I, f, and ℓ, up to the current level of approximation these are all good quantum numbers. Then a rovibronic eigenstate corresponding to vibrational number v, in a single channel, can be designated by $|\beta, v, FM_F\rangle$, where β represents $[(SI)f, \ell]$ and as above $\mathbf{F} = \mathbf{f} + \boldsymbol{\ell}$. The corresponding eigenfunction would be written as a sum over the $|R_i\rangle$ computational basis states: $|\beta, v, FM_F\rangle = \sum_i |R_i\rangle\langle R_i|\beta, v, FM_F\rangle$. The β notation incorporates the effect of nuclear spins into the notation used above, namely $|\eta\,\ell, v\rangle$, where $\eta = a(X)$ for $S = 1(0)$. In the remainder of the paper, all expressions for wavefunctions and matrix elements are written in terms of the computational basis, which we sometimes write in the unfactorized form $|R_i \beta v F M_F\rangle$.

The precision of the data requires also a consideration of mixing between these channels induced by the hyperfine interactions, and by second-order spin-orbit effects. These effects are needed to explain small splittings between levels with identical values of ℓ and f, but different values of F. These mixings are independent of M_F, so we suppress this quantum number through expressions in the rest of this section.

Singlet-triplet coupling by hfs effects can be derived by transforming the hyperfine Hamiltonian from the case $e_{fafb,f}$ atomic limit to the molecular regime, which we denote $e_{SI,f}$ by contrast. (The $e_{SI,f}$ representation is identical with the b_β case of [47].) The transformation between $e_{SI,f}$ and $e_{fafb,f}$ is well known:

$$\begin{aligned}\langle (S_a,S_b)S,(I_a,I_b)I,f|(S_a,I_a)f_a,(S_b,I_b)f_b,f\rangle \\ = [(2f_a+1)(2f_b+1)(2S+1)(2I+1)]^{1/2} \\ \times \left\{ \begin{array}{ccc} S_a & I_a & f_a \\ S_b & I_b & f_b \\ S & I & f \end{array} \right\} = T(e_{SI,f}, e_{fafb,f}), \end{aligned} \quad (11)$$

where the quantity in brackets is a $9J$ symbol. When rotation is considered, the molecular case $e_{SI,f}$ basis set becomes $|[(S,I)f,\ell]FM_F\rangle$, as stated above.

The above transformation, applied to H_{hf} (Eq. 8), yields the form $\mathbf{I}\cdot\mathbf{S}$ given in Eq. 10 plus additional terms that couple S=0 and 1. In the computational basis, the matrix elements of H_{hf} can be written

$$\langle R_i v|\langle[(SI)f,\ell]F|H_{hf}(f_a,f_b)|[(S'I')f',\ell']|v'R_j\rangle \quad (12)$$

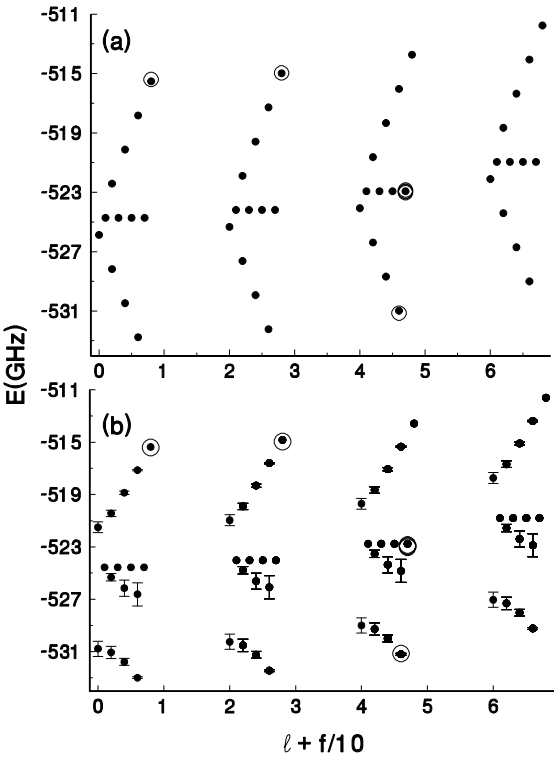

FIG. 5: Energy levels calculated for the $v_a = 37$ band, from (a) the uncoupled hyperfine structure expression, Eq. (10), not including singlet states; and (b) from calculations with the $|[(S,I)f,\ell]FM_F\rangle$ basis, including singlet-triplet mixing (only even ℓ values are shown). Filled circles are calculated values, open circles denote experimental values, and error bars denote the fraction of singlet character in (b), with the maximum length corresponding to 100%.

$$\begin{aligned} &= \sum_{f_a,f_b} T(e_{SI,f}, e_{fafb,f}) H_{hf}(f_a f_b) T^\dagger(e_{S'I',f'}; e_{fafb,f'}) \\ &\times\ \delta_{f,f'}\delta_{F,F'}\delta_{\ell,\ell'}\delta_{i,j}\delta_{v,v'} = \delta_{f,f'}\delta_{F,F'}\delta_{\ell,\ell'}\delta_{i,j}\delta_{v.v'} \\ &\times\ \left\{ \frac{A_a}{2}(\mathbf{I}\cdot\mathbf{S})\delta_{S,S'}\delta_{I,I'} + (\Delta S = \pm 1 \ \text{ terms}). \right\} \end{aligned}$$

The $\Delta S = 0$ terms are nonzero only for $S = 1$, and have $I = I'$. The $\Delta S = \pm 1$ terms have $I' = I \pm 1$. We have not been able to obtain a simple analytic expression for the $\Delta S \neq 0$ terms.

The second-order spin-orbit terms (H_{SO2}) have the same quantum number dependence [48] as spin-spin magnetic dipole terms, which themselves can be estimated to be negligibly small (< 1 kHz) for the Cs_2 $a^3\Sigma_u^+$ state. Of several possible representations for the H_{SO2} terms, the simplest uses a basis of values of the projection of the spin angular momentum along the internuclear axis, $\hat{n}$. We denote the projections along $\hat{n}$ of $\mathbf{S}, \mathbf{I}$, and $\mathbf{F}$, by Σ, ι, and ϕ, respectively. We can then define the represen-

TABLE I: Possible values for the f quantum number for the Cs_2 X and a states, and corresponding values of f_a, f_b, I, S and $\mathbf{I}\cdot\mathbf{S} = (1/2)[f(f+1) - S(S+1) - I(I+1)]$.

f	$[f_a, f_b]$	$[S, I]$	$\mathbf{I}\cdot\mathbf{S}$ (for $S=1$)
		Even ℓ	
0	[3,3],[4,4]	[1,1],[0,0]	-2
1	[3,4]	[1,1]	-1
2	[3,3],[3,4],[4,4]	[0,2],[1,1],[1,3]	1,-4
3	[3,4]	[1,3]	-1
4	[3,3],[3,4],[4,4]	[0,4],[1,3],[1,5]	3,-6
5	[3,4]	[1,5]	-1
6	[3,3],[3,4],[4,4]	[0,6],[1,5],[1,7]	5,-8
7	[3,4]	[1,7]	-1
8	[4,4]	[1,7]	7
		Odd ℓ	
1	[3,3],[3,4],[4,4]	[0,1],[1,0],[1,2]	-3
2	[3,4]	[1,2]	-1
3	[3,3],[3,4],[4,4]	[0,3],[1,2],[1,4]	2,-5
4	[3,4]	[1,4]	-1
5	[3,3],[3,4],[4,4]	[0,5],[1,4],[1,6]	4,-7
6	[3,4]	[1,6]	-1
7	[3,4],[4,4]	[0,7],[1,6]	6

tation a_α with basis states $|S, I, \Sigma, \iota, p, F, \phi\rangle$, as in [48], where p denotes the parity ($p = (-1)^\ell$ in the $e_{SI,f}$ basis), and $\phi = \Sigma + \iota$ is nonnegative. In this a_α basis, H_{SO2} is diagonal, depends only S and Σ, and has nonzero matrix elements only for S=1:

$$H_{SO2}(R; S, \Sigma) = \frac{2}{3}\lambda_{SO2}(R)[3\Sigma^2 - S(S+1)]. \quad (13)$$

For $\lambda_{SO2}(R)$ we have used a function of the form used in [40]:

$$\lambda_{SO2}(R) = S_{SO2}\ 10^{(-\beta_{SO2}R)}. \quad (14)$$

Note that often, as in [49], one writes λ_{SO2} as a function of v: $\lambda_{SO2}(v) = (1/2)[E(^3\Sigma^+_{1u}, v) - E(^3\Sigma^+_{0u}, v)]$. However, in our multi-channel DVR formulation, the R-dependent form is more appropriate.

The transformation from the molecular case $e_{SI,f}$ basis to the a_α basis is given by a product of two Clebsch-Gordan coefficients, as derived in [38]:

$$\begin{aligned} T(e_{SI,f}; a_\alpha) &= \langle[(S,I)f,\ell]F|S, I, \Sigma, \iota, p, F, \phi\rangle \\ &= (-1)^{\ell-F-\phi}[1 + (-1)^{\ell+p}][2 - \delta_{\Sigma 0}\delta_{\iota 0}]^{-1/2} \\ &\quad \times \langle S, \Sigma, I, \iota|f, \phi\rangle\langle f, -\phi, F, \phi|\ell 0\rangle. \end{aligned} \quad (15)$$

We transform $H_{SO2}(R; S, \Sigma)$ from the a_α representation to the $e_{SI,f}$ representation to find matrix elements in the computational basis:

$$\begin{aligned} &\langle R_i v|\langle[(SI)f,\ell]F|H_{SO2}(R, S, \Sigma)|[(S', I')f', \ell']F'\rangle|v' R_j\rangle \\ &= \sum_{a_\alpha} T(e_{SI,f}; a_\alpha) H_{SO2}(R_i; S, \Sigma) T^\dagger(e_{S'I',f'}; a_\alpha) \\ &\times\ \delta_{S,S'}\delta_{I,I'}\delta_{F,F'}\delta_{i,j}\delta_{v,v'}\delta_{v,v'} \end{aligned} \quad (16)$$

We can now calculate orthogonal transformations between the three basis sets, $e_{fafb,f}$, $e_{SI,f}$, and a_α, each with the same number of basis states. For even ℓ and $F \geq f$ there are at most 72 possible basis states, since ℓ can range from $F - f$ to $F + f$. Each channel requires at least 350 mesh points in R for the multichannel DVR eigenvalue calculations for the data considered here. (A larger range of R is required for the data of [18]). To reduce the scale of the calculation, we acknowledge that the data comes from only f = 8, 9, and 10, and states with $\ell > 6$ are very weakly coupled to levels of interest. (There are near degeneracies between $\ell = 4$ and $\ell = 6$ levels.) Thus the calculation is restricted to $0 \leq \ell \leq 6$. This reduces the number of channels from 72 to 28 for $F = 8$, and somewhat fewer for $F = 10$.

In the computational basis, neither the $\Delta S = \pm 1$ terms of H_{hf}, nor H_{SO2} (which mixes states of given ℓ and f), are diagonal. Hence eigenfunctions of the multi-channel DVR matrix for a given value of F, M_F are R-dependent rovibronic states of mixed $\beta F \equiv |[(SI)f, \ell]F\rangle$ character. The final eigenstates, while not vibrational levels of a single potential, can be enumerated by index k and will be designated by $|k, F, M_F\rangle$. (M_F will be omitted in what follows.) The eigenfunctions can be written $\sum_{i,\beta} |R_i\beta\rangle\langle R_i\beta|kF\rangle$. Franck-Condon overlaps, for example, will be given by $\sum_{i,\beta}\langle k, F|R_i\beta\rangle\langle R_i\beta|k', F\rangle$. Note that among those states observed in the experiments reported here, intermixing of ℓ and f values is typically less than a 10% effect. The $v_a = 37$, F=10 (ℓ, f)=(4,7) and =(6,6) doublet, which is nearly a 50-50 mixture of X and a state character, represents an exceptional case.

V. RESULTS

One of our objectives is to observe levels of the Cs_2 $a^3\Sigma^+_u$ state moderately close to the dissociation limit and attempt to detect the presence of nearby levels of the $X^1\Sigma^+_g$ state, so as to lead to precise measurements of the relative binding energies.

A least squares fitting process is used to optimize parameters to reproduce the experimental data. Table II lists the measured binding energies (which have experimental uncertainties of 0.34 GHz to 0.42 GHz) and energy level differences (experimental uncertainties of 30 MHz), and shows the quality of the fit. The fitted parameters are the a state potential parameters, D_e, R_e and the a_i parameters, the $SO2$ parameters S_{SO2} and β_{SO2}, and also parameters that applied to both the X and the a states, such as C_6, C_8, and the exchange parameters $A_{\rm exch}, \gamma_{\rm exch}$ and $\beta_{\rm exch}$. The parameters accepted from other sources and the fitted parameters are given in Tables III, IV and V. The calculated binding energies are within or nearly within the quoted uncertainty of the experimental value. The fitted energy differences with respect to the anchor levels exhibit a root mean square (rms) residual of 90 MHz, and in some cases are as large as 7 times the experimental uncertainty of 30 MHz, in

TABLE II: Observed and calculated binding energies, E_b, and difference energies, ΔE, in GHz. Binding energies (with experimental uncertainties in the σ column) are given only for the $(\ell, f)F$ =(0,8)8 "anchor levels" in each band. Observed difference energies between the anchor levels and other $(\ell, f)F$ levels are given in the next to last column, while difference between the observed and calculated ΔE values are given in the last column. The experimental uncertainties for all of the ΔE values are 0.030 GHz. Levels of the degenerate, strongly mixed pair of nominal $\left[a^3\Sigma_u^+\right](4,7)\,10$ and $\left[X^1\Sigma_g^+\right](6,6)\,10$ states that are discussed in the text and depicted in Figs. 7(b) and 8 are denoted by * ((4,7)10 is the major component in each case). The calculated level positions for each state in this pair corresponds to the nearest level shown in Fig. 7(b).

(0,8)8 anchor level binding energy, E_b				Energy difference from anchor level, ΔE		
v_a	obs	obs-cal	σ	$(\ell, f)F$	obs	obs-cal
28	-1490.855	-0.25	0.39	(2,8)10	0.621	-0.020
29	-1354.275	0.19	0.34	(2,8)10	0.600	-0.025
				(2,8)10	0.578	-0.030
				(4,7)9	-6.975	0.096
30	-1224.670	0.13	0.42	(4,7)10	-7.000	-0.021
				(4,7)8	-7.075	0.011
				(2,7)9	-8.185	0.167
				(4,6)10	-15.006	0.030
				(2,8)10	0.564	-0.027
31	-1102.195	0.11	"	(4,7)9	-6.911	0.219
				(4,6)10	-14.923	0.192
				(2,8)10	0.448	-0.035
				(4,7)10*	-7.446	0.012
37	-515.405	0.24	"	(4,7)8	-7.528	-0.020
				(4,7)9	-7.550	-0.062
				(4,7)10*	-7.625	0.073
				(4,6)10	-15.731	0.109
				(2,8)10	0.434	-0.029
				(4,7)10	-7.469	0.053
38	-441.285	-0.29	"	(4,7)8	-7.508	0.080
				(4,7)9	-7.538	0.042
				(4,6)10	-15.549	0.110

defiance of repeated least square fitting efforts. By contrast, the rms residual for the $\mathbf{I}\cdot\mathbf{S}$ model is 180 MHz, which is surprisingly good considering it's simplicity.

Our experimental data yielded well-resolved rotational and hyperfine structure. The rms shifts from the second-order spin-orbit interaction (SO2) were 120 MHz, or somewhat larger than the experimental resolution. We note that the data from [12] were important because, although of relatively low resolution, they establish the a state potential minimum. From the combined fit, the rms residual for just the data of [12] was 0.34 cm^{-1}, a value that is comparable to the expected spread of hyperfine structure, which was not resolved in those experiments.

TABLE III: Summary of molecular constants for the Cs_2 $X^1\Sigma_g^+$ and $a^3\Sigma_u^+$ states. The hfs center of gravity, 0.34496 cm^{-1} above the $f_a + f_b$ = 3+3 atomic limit, is taken as the dissociation limit in our work.

	D_e (cm^{-1})	ω_e (cm^{-1})	R_e (Å)
	$X^1\Sigma_g^+$		
Danzl *et al.*[23]	3650.0321(14)		
Amiot,Dulieu [19]	3649.88(45)	42.021303	4.645160
Krauss,Stevens [50]	3573.	40.99	4.625
	$a^3\Sigma_u^+$		
This work	279.23(4)	11.63	6.330(10)
Xie *et al.* [12]	279.35(5)	11.6336	6.2354(76)
Magnier/Li [11]	295	11.58	6.303
Aubert-Frécon [51]	255.6		6.36
Krauss,Stevens [50]	282	11.29	6.265
Foucrault *et al.* [52]	233	10.50	5.556
"	267	11.86	6.276

TABLE IV: C_6, C_8 and exchange parameters used in the fit to the data. All values are in atomic units, where for C_n, the atomic unit is 1 $E_H a_0^n$, with $E_H = 4.3597442 \times 10^{-18}$ J, and $a_0 = 5.29177211 \times 10^{-11}$m. For $A_{\rm exch}$, the atomic unit is $E_H a_0^{-\gamma_{exch}}$. p.w.=present work. Numbers in brackets in the last two columns indicate the decimal exponent.

		C_6	C_8	$A_{\rm exch}$
[53](1995)	Th.	6331.	9.630[5]	
[54](1999)	Th.	6851.(54)		
[16](2000)	Ex.	6890.(35)	9.546[5]	
[19](2002)	Ex.	6836.(100)	9.63(19)[5]	1.10[-3]
[18](2004)	Ex.	6846.2(137)	9.63[5]	1.187(86)[-3]
[17](2004)	Ex.	6860.(25)	8.60(75)[5]	
p.w.		6816(34)	9.6302[5]	1.2286[-3]

The relative position of hyperfine levels calculated from the simple form, $H_{hf} = (A_{hf}/2)\mathbf{I}\cdot\mathbf{S}$, is identical for each vibrational level. Fig. 6 shows that for $v_a = 38$, the energy levels differ only slightly from the $(A_{hf}/2)\mathbf{I}\cdot\mathbf{S}$ representation even though there is a singlet state lying just above. On the other hand, Fig. 5 for $v_a = 37$ shows substantial shifts in some of the calculated energy levels, although the *observed* triplet state levels (denoted by open circles) are perturbed to a smaller degree. In both figures, the length of the error bars denotes the singlet fraction: the longest bars indicate essentially 100% singlet character.

The variation of energy with F and the shifts due to the SO2 term for the $v_a = 37$ band are displayed in more detail in Fig. (7), vs. $\ell + f/10 + F/200$. In this plot, the $\times$ symbols denote results with no SO2 (independent of F), the dots with SO2. Evidently certain (ℓ, f) levels are affected more than others, but in general the shifts due to SO2 are much smaller than the hyperfine effects. The presence of a singlet state in the experimental data is in-

TABLE V: Other parameters used in the fit to the data. $\gamma_{\rm exch}$ and b are dimensionless, $\beta_{\rm exch}, C_{10}$ and C_{12} are in a.u., β_{SO2} is in Å^{-1}, and S_{SO2} as well as the a_i are in cm^{-1}. The parameters attributed to [40] were obtained by a simulation/approximation of the results plotted in this work with a simple function decaying exponentially with R.

		Source
$\gamma_{\rm exch}$	5.542	[19]
$\beta_{\rm exch}$	1.070	[19]
C_{10}	1.35912[8]	[53]
C_{12}	2.901[10]	[53]
S_{SO2}	237.8	[40]
β_{SO2}	0.4783	[40]
S_{SO2}	660.	p.w.
β_{SO2}	0.4022	p.w.
b	0.100	p.w.
a_2	6.2942102727[3]	p.w.
a_3	-1.2870429705[4]	p.w.
a_4	-2,8509013445[4]	p.w.
a_5	-1.4276716944[5]	p.w.
a_6	2.3201276928[6]	p.w.
a_7	-4.4143616446[6]	p.w.
a_8	-2.3166781429[7]	p.w.
a_9	1.1626864521[8]	p.w.
a_{10}	-1.9006036858[8]	p.w.
a_{11}	1.1022364715[8]	p.w.

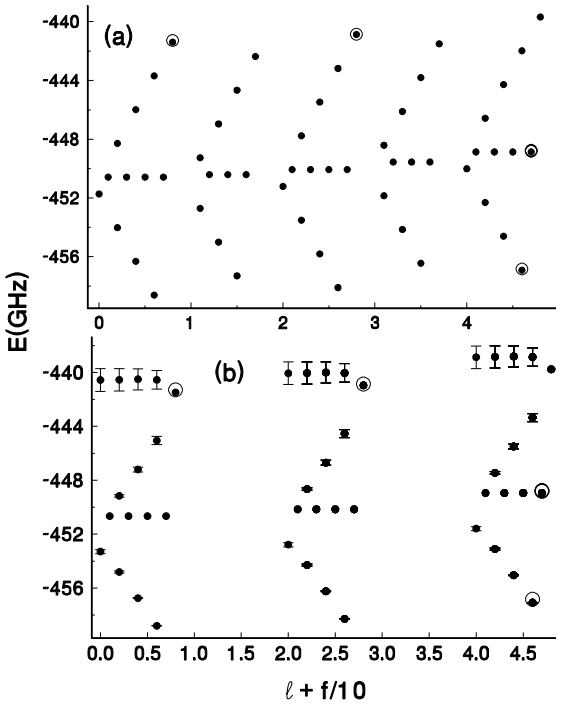

FIG. 6: Energy levels calculated for ℓ=0-4 levels of the v_a = 38 band from fitted parameters, from (a) the uncoupled hyperfine structure expression, Eq. (10), without singlet states; and (b) from calculations with the $|[(S,I)f,\ell]FM_F\rangle$ basis, including singlet-triplet mixing and H_{SO2} terms. Small filled circles are calculated values, open circles denote experimental values, and error bars denote the fraction singlet character in (b). In (b), the nearby singlet state mixes slightly with triplet state levels f = 0 and 6, especially.

dicated primarily by the $v_a = 37, F = 10, (\ell, f) = (4, 7)$ doublet. Fig. 7b shows on a finer scale the energies for F=8, 9 and 10, and for $(\ell, f) = (4, 7)$ and (6,6), which are superimposed in this figure. By varying the potential parameters and the magnitude of S_{SO2}, we established that H_{SO2} couples $(\ell, f)F$ = (4,7)10 and (6,6)10, by 40 MHz - 80 MHz. Evidently these two states share enough (4,7)10 character to produce the doublet observed experimentally, as discussed in [1]. In Table II, the residual for the lower of the two nominally v=37, (4,7)10 levels is obtained from the energy for the calculated (6,6)10 level, in accord with the level configuration indicated in Fig. 7b.

Another perspective on the F=10 doublet is provided by Fig. (8), from Ref. [1]. This shows that for v=37, a doublet appears for σ^- polarization, while for v=38, there is a single peak for this polarization. (The apparent doublet observed in both bands for σ^+ polarization comes from levels of different F values.) The observed v=37, F=10 doublet splitting is 179(20) MHz, and since the two peaks are of nearly equal amplitude, one concludes that 179 MHz is very nearly twice the effective coupling parameter between two nearly degenerate levels. The splitting in the calculated values, shown in Fig. (7), is only 122 MHz. To obtain a larger splitting required larger values of λ_{SO2} for v=37, but larger values of λ_{SO2} produced deviations from other observed level differences in v=30 and 31. The fit results shown in Tables II - V are thus a compromise between even larger deviations in the binding energies for v=31, and larger deviations of the v=37 F=10 doublet splitting. This same dilemma was obtained not only for the piecewise potential using equations 2 and 3, but also for the Morse Long Range potentials which were based on an entirely different representation. Evidently our model is somehow deficient, but we have not been able to identify the origin of the problem.

Since energies calculated in the (ℓ, f) representation are independent of F, the question arises why a doublet is not observed for F = 8 and 9. Our analysis of the calculated energy level structure indicates that for F = 8 and 9, the mixing is somewhat less because the matrix element is slighly smaller. The calculated (6,6) fraction decreases from about 0.40 in F = 10, to 0.15 in F=9 and 0.07 in F=8. These numbers show the extreme sensitivity of this feature to the molecular parameters, and suggest that this observed doublet rather precisely locates

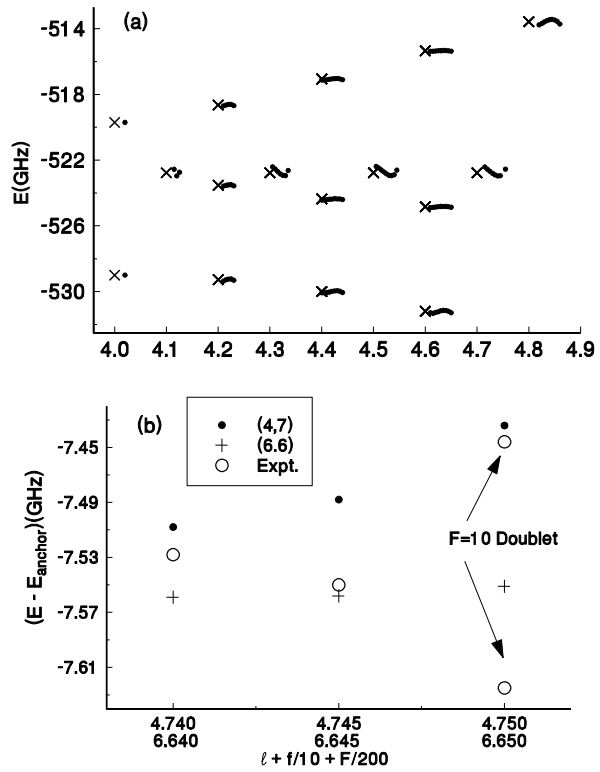

FIG. 7: Energy levels calculated and observed for the v=37 band. In (a), the × symbols denote energies calculated without second-order spin-orbit effects, filled circles with. In (b), we compare energies calculated for (ℓ, f) =(4,7) (filled circles) and for (6,6) (pluses) in order to show their near degeneracy. The experimental data for the nominally (4,7) band are shown as open circles. The values calculated for (6,6) are shifted along the x axis by 2.1 in order to superimpose them on the (4,7) values. All data have been referenced to the v=37 anchor level, calculated or observed, respectively.

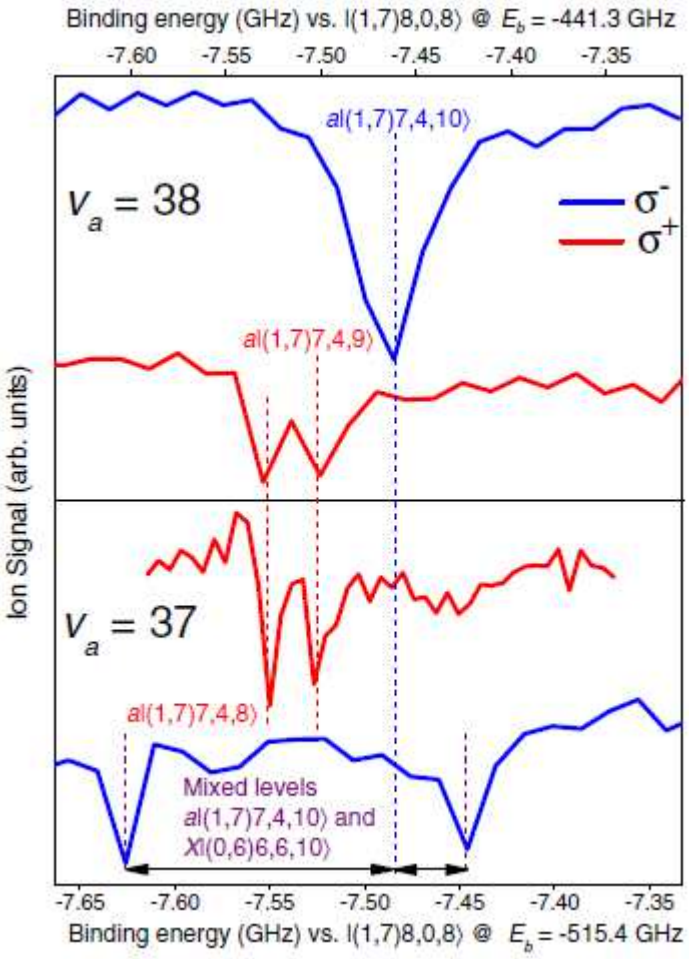

FIG. 8: (In color online.) This figure, from [1], shows parts of the experimental data scans for v=37 and 38. For v=37, there is a doublet for $(f, \ell)F$ =(7,4)10 that is not present for v=38. See text for further discussion.

the v=138 singlet vibrational level relative to the triplet state v=37 level. Figure 9a shows that near degeneracies between singlet and triplet levels exist in v=33, although there are no appreciable perturbative interactions here.

We note also that the singlet-triplet wavefunction overlap between nearly degenerate levels decreases as one moves down in energy because the potentials diverge, as shown in Fig. 4. That the singlet-triplet coupling is sensitive to the wavefunction overlap also enters significantly in model calculations of the splittings of X state levels reported in [22]. The splittings for ℓ=15 of v_X = 137 that we calculate from our parameters are only about 42% the experimental values reported in [22], and we attribute this to slight deficiencies of our potentials and the extreme sensitivity to wavefunction overlaps.

It would have been desirable to include in the fit the precision data from Ref. [18] for levels within 2.5 cm^{-1} of the dissociation limit as well as Feshbach resonance data from [13–15]. However the additional number of mesh points in R, as well as the large number of $[(S, I)f, \ell]F$ channels coupled by H_{SO2} made this impractical. Actually, the effect of H_{SO2} on the data of [18] is quite small. If the H_{SO2} terms are dropped, our methods with full rather than truncated wavefunctions in R, yielded a reasonable simulation of the data of [18], as shown in Fig. 9b. We note also that these data near the dissociation limit are not so useful for making measurements sensitive to m_e/m_p: as described in [1], the sensitivity to changes in m_e/m_p decreases to zero near the dissociation limit.

VI. IMPLICATIONS FOR MEASUREMENTS SENSITIVE TO CHANGES IN m_e/m_p.

The data presented here and discussed in [1] exposed one instance in which a small amount of singlet-triplet mixing produces a state of nearly equal singlet-triplet character, hence an unexpected doublet in the spectrum.

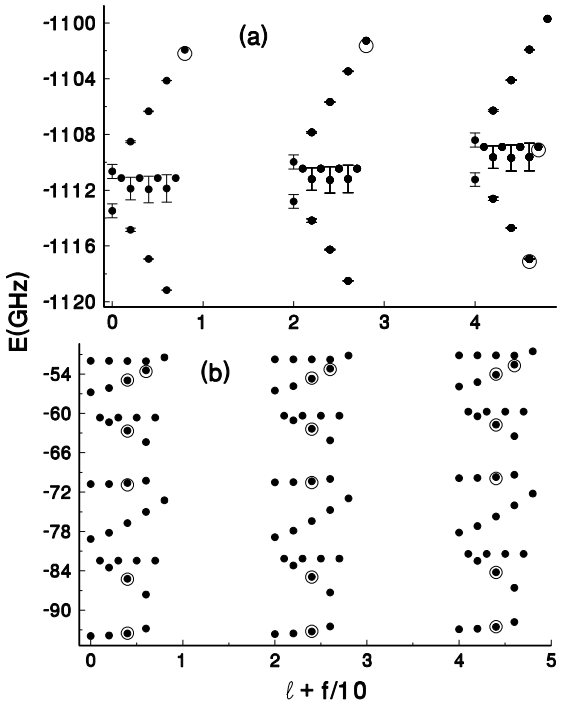

FIG. 9: Energy levels calculated with the $|[(S,I)f,\ell]FM_F\rangle$ basis, for (a) the $v_a = 31$ band and (b) for data reported by [18], closer to the dissociation limit. As above, error bars in (a) represent the fraction of singlet character.

This can be used to determine the relative position of singlet and triplet levels. Because the singlet potential is much deeper than the triplet potential, measurements of the splitting between a pair of X and a state levels that lie near to each other would be sensitive to $\mu = m_e/m_p$, as discussed in [1]. Ref. [1] proposed some specific pairs of levels in Cs_2 that appear promising for such measurements. The level structure obtained here from fits to the data suggests that there may be other avenues to the same goal, depending on available experimental techniques.

In Ref. [1], it was proposed to use microwave (MW) spectroscopic techniques to measure the small splitting between such a pair of close-lying levels. Use of ultracold molecules for such experiments would allow for the longest possible observation time and hence best energy resolution. We consider in particular an atomic fountain-type experiment, where MW linewidths $\Gamma \approx 1$ Hz are typical. To perform such measurements, a superposition of the levels of interest must be created; this in turn requires that three steps be experimentally viable: a) a method to initially populate one of the levels; b) a method to coherently couple them (i.e. drive transitions between them with $\pi/2$ pulses); and c) a method to selectively detect one of them. In this section we discuss the viability of these three steps for specific cases of nearly-degenerate a and X state levels in Cs_2.

In the case of the alkali dimers, and Cs_2 in particular, methods such as photoassociation (e.g. [1, 8]) and/or magnetoassociation plus stimulated Raman transfer [10, 60] have been shown capable of producing a wide range of molecular bound states in the ultracold regime. Hence, we assume that states of the type produced in these experiments (primarily with low, even values of ℓ) can be produced at will. In addition, state-selective detection with sufficient resolution has been demonstrated in similar states of ultracold alkali dimers, e.g. in Rb_2 [10]. Hence, we also assume that detection can be accomplished with standard methods.

We note one caveat to these assumptions: namely, that it is highly advantageous to consider transitions between sublevels that are insensitive to magnetic fields at first order, i.e. where both initial and final states have $M_F = 0$. However, in most experiments where ultracold molecules are formed, either near-extreme M_F sublevels are created (as in the experiments reported here), or the distribution of M_F populations is not controlled (e.g. when molecules are formed by photoassociation from an unpolarized atomic sample). In the latter case, the $M_F = 0$ level and $\Delta M_F = 0$ transition likely could be selected by the high-resolution MW spectroscopy; however this would come at the expense of signal size since only a small fraction of population would reside in the desired $M_F = 0$ initial state. We believe it is likely possible to selectively create molecules in a $M_F = 0$ state using coherent transfer methods, but to our knowledge this has not yet been demonstrated experimentally. While using states with $M_F \neq 0$ is conceivable in principle, in general this would require stabilization of magnetic fields in the experiment at a level that is technically very challenging. For completeness, we consider both possibilities in the ensuing discussion.

We next focus on step b) above: the requirement to drive transitions between pairs of close-lying levels in the $a^3\Sigma_u^+$ and $X^1\Sigma_g^+$ states. We consider specificially the amplitudes for driving direct, MW-frequency transitions between such pairs. We note that both electric dipole (E1) and magnetic dipole (M1) transitions between these levels are nominally forbidden: for E1 transitions this is due to the change in S, while for M1 transitions this is due to the change $u \leftrightarrow g$. However, both types of transitions are allowed due to mixings with other levels, such that S and u/g are not exact quantum numbers (see below).

Electric dipole transitions. We have used two different approaches to determine the E1 dipole moment. One is based on a non-perturbative relativistic electronic-structure calculation and a second relies on a perturbative evaluation based on eigenfunctions of the non-relativistic electronic Hamiltonian and matrix elements of the spin-orbit interaction between the X and a state

and excited electronic states.

In order to determine the strength of the relativistic transition dipole moment between the $X^1\Sigma_g^+(\Omega = 0)$ and $a^3\Sigma_u^+(\Omega = 1)$ states non-perturbatively, we performed a fully relativistic *ab-initio* calculation using a restricted active space configuration-interaction (RAS-CI) method [56, 57] with single, double, and triple excitations. The extended basis set, constructed from Dirac-Fock and Sturm's orbitals, include $5p^6$ core, $6s$, $6p$ valence and $5d$, $4f$ virtual excitations. We find that a significant part of the binding energy of and the dipole moment between these states is due to correlation effects between core and valence electrons. These correlations have a strong dependence on internuclear separation. Figure 10 shows our transition dipole moment as a function of internuclear separation R. The dipole moment is well represented by a sum of two exponentials for $R > 4.2\mathring{A}$. That is,

$$d(R) = \sum_{i=1,2} A_i e^{-\kappa_i R} \tag{17}$$

with $A_1 = 0.17017$ Debye and $A_2 = 41.273$ Debye. (One Debye = 3.3362×10^{-30} Coulomb m). Moreover, $\kappa_1 = 0.31348$ Å^{-1} and $\kappa_2 = 1.81865$ Å^{-1}.

We use the ro-vibrational wavefunctions $\psi_{\eta,v\ell}(R) = \langle R|\eta, v\ell\rangle$ of $H_{BO,\eta} + H_{kin} + H_{rot}$, computed in the discrete variable representation, and the analytical representation of the dipole moment to find the rotationally and vibrationally-averaged dipole moment $d_{vv'} = \langle a, v\ell|d(R)|X, v'\ell'\rangle\delta_{\ell,\ell'\pm1}$. Figure 11 gives a plot of $d_{vv'}$ for the $v = 37$ and $v = 38$ vibrational levels of the $\ell = 0$ $a^3\Sigma_u^+$ state as function of the vibrational levels of the $\ell' = 1$ $X^1\Sigma_g^+$ state. Typically, the dipole moment is on the order of 10^{-3} Debye, while for $v' > 140$ it quickly approaches zero. Values for $d_{vv'}$ for selected vv', for which the binding energies of the $X^1\Sigma_g^+$ and $a^3\Sigma_u^+$ levels are nearly degenerate, are given in the caption.

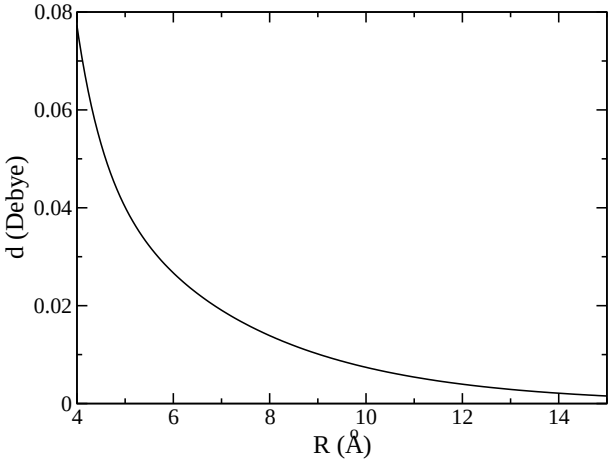

FIG. 10: The non-perturbative electronic transition dipole moment between the relativistic $X^1\Sigma_{0g}^+$and $a^3\Sigma_{1u}^+$ states of the Cs_2 molecule as a function of internuclear separation.

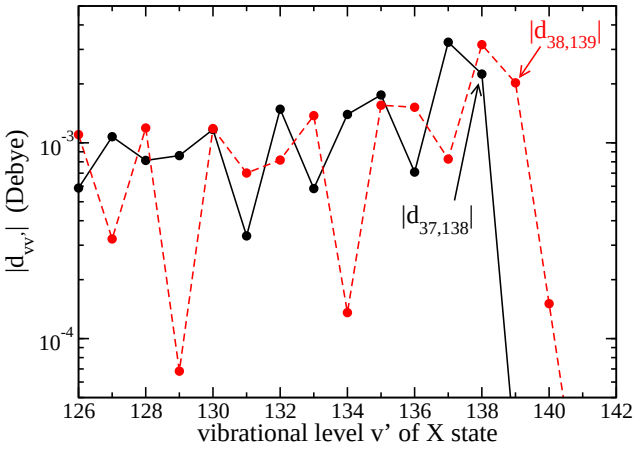

FIG. 11: (In color online.) The vibrationally-averaged transition dipole moment, $|d_{v,v'}|$ for the vibrational levels $v = 37$ (black solid curve) and 38 (red dashed curve) of the $\ell = 0$ a $^3\Sigma_u^+$ state as a function of the vibrational level v' of the $\ell' = 1$ $X^1\Sigma_g^+$ potential. We find transition dipole moments $|d_{37,138}| = 2.2 \cdot 10^{-3}$ Debye and $|d_{38,139}| = 2.0 \cdot 10^{-3}$ Debye.

Perturbative results are smaller than those of the relativistic calculation. This is consistent with findings on the size of the second-order spin-orbit interaction H_{SO2}. There the perturbative results were also found to underestimate the physical values [13, 40, 58].

To estimate angular factors for electric dipole transitions between states that are primarily $X^1\Sigma_g^+$ and those that are primarily $a^3\Sigma_u^+$, we employ the result of the (less-exact) perturbation approach which concludes that the leading term that produces an allowed E1 transition between these states is spin-orbit mixing between $a^3\Sigma_{1u}^+$ and a higher $^1\Pi_u$ state. We therefore assume a perturbative mixing $\tilde{a}^3\Sigma_{1u}^+ = \alpha a^3\Sigma_{1u}^+ + \beta^1\Pi_u$, where $|\alpha|^2 + |\beta|^2 = 1$. Thus the "angular factor" will introduce a quantity proportional to β to multiply the $d_{vv'}$ values obtained in the above discussion.

It will be simplest to evaluate the E1 transition in the a_α representation, using Eq. (15) to transform to $e_{SI,f}$. To summarize what follows, we can write

$$\begin{aligned}\langle X^1\Sigma_g^+|\mu \cdot E|\tilde{a}^3\Sigma_u^+\rangle/E &= \beta T(X; a_\alpha(X)) \\ &\times\langle a_\alpha(X)|\mu|a_\alpha(^1\Pi_u)\rangle T(a_\alpha(^1\Pi_u);^1\Pi_u)^\dagger.\end{aligned} \tag{18}$$

where the T elements indicate the $T(e_{SI,f}; a_\alpha)$ transformations as given in Eq.(15).

We will consider only $M_F = 0$ elements to avoid spurious Zeeman shifts if the experimental magnetic field is not zero. Matrix elements of μ in the a_α representation follow from a slight extension of Eq. 6.320) of [48] to obtain an expression for $\Delta\Lambda = \Delta\Omega = 1$ (here F is even, so $(-1)^{2F} = 1$):

$$\begin{aligned}\langle a_\alpha(X)|\mu|a_\alpha(^1\Pi_u)\rangle = \langle S = 0, I, \Sigma = 0, \Lambda = 0, \iota, p, F, \phi, \\ M_F = 0|\mu|S' = 0, I' = I, \Sigma' = 0, \Lambda = 1, \iota' = \iota, p' = -p,\end{aligned}$$

$$F'\phi' = \phi+1, M_F=0\rangle = d_{vv'} \begin{pmatrix} F & 1 & F' \\ 0 & 0 & 0 \end{pmatrix} (-1)^{\phi} \times \begin{pmatrix} F & 1 & F' \\ -\phi & -1 & \phi+1 \end{pmatrix} [(2F+1)(2F'+1)]^{1/2} \quad (19)$$

For transitions between $M_F = 0$ sublevels, we will have $F = F' \pm 1$. After applying $T(e_{SI,f}; a_\alpha)$ from Eq. (15) to both sides, the result, without the factor β, will be a rough estimate of the angular factors that multiply the $d_{vv'}$ quantities obtained above. Numerically, we find that the μ matrix element values are no more than 0.5, while the transform elements are each no more than 0.3. However, in view of the sum over $\iota(-I \le \iota \le I)$, the net effect of the transform elements is of order unity. Therefore the angular factors reduce the effective dipole transition strength by a factor of 2 to 3.

An E1 transition dipole moment of 1×10^{-3} Debye would produce a transition rate of $\Omega_{E1} \approx 3 \times 10^3$/s for a MW electric field with amplitude of 1 V/cm. Since $\Omega_{E1} \gg \Gamma$ (where $\Gamma \sim 2\pi \times 1$ Hz is the Ramsey linewidth in the fountain), this would likely be adequate to measure the energy splitting between such pairs of states in an atomic fountain experiment with a MW cavity.

Magnetic dipole transitions. Magnetic dipole transitions are allowed between nominal $a^3\Sigma_u^+$ and $X^1\Sigma_g^+$ states, due to H_{hf}-induced mixing of a components into the X states. The M1 transition amplitude between these initial and final states is determined by the perturbing Hamiltonian $H'_{M1} = -g_e\mu_B \mathbf{S}\cdot\mathbf{B}$, where $g_e \approx 2$ is the electron g-factor; μ_B is the Bohr magneton; $\mathbf{B}$ is an, oscillating magnetic field; and we ignore much smaller contributions due to nuclear and other magnetic moments. We consider the case of transitions between specific eigenstates of the total Hamiltonian, initial state $|FM_F,k\rangle$ and final state $|F'M'_F,k'\rangle$, driven by a linearly polarized B-field $\mathbf{B} = B\hat{z}\cos\omega t$.

In order to calculate the transition moment $M_{M1} = \langle F'M'_F,k'|H_{M1}|FM_F,k\rangle/B$, we use the expression for the total wavefunction over the grid points R_i and channels, β: $|FM_F,k\rangle = \sum_{i,\beta}|R_i\rangle|\beta\rangle\langle R_i\beta|F,M_F,k\rangle$, where $\beta = (S,I)f\ell$ as before. Then the transition amplitude in the rotating frame is

$$\langle F'M'_F,k'|M_{M1}|FM_F,k\rangle = -\frac{g_e\mu_B}{2} \times \sum_{i,\beta',\beta} \langle F',M'_F,k'|\beta'R_i\rangle \times\langle[(S',I')f',\ell']F'M'_F|S_z|[(S,I)f,\ell]FM_F\rangle \times\langle R_i\beta|F,M_Fk\rangle. \quad (20)$$

The angular part of the matrix element can be evaluated using standard transformations, taking into account that S_z does not act on I or ℓ, and that it has nonzero matrix elements only when $S = S' = 1$. We find

$$\langle[(S',I')f'\ell']F'M'_F|S_z|[(S,I)f,\ell]FM_F\rangle = (-1)^Q\sqrt{6(2F+1)(2F'+1)(2f+1)(2f'+1)} \times \begin{Bmatrix} f' & F' & \ell \\ F & f & 1 \end{Bmatrix} \begin{Bmatrix} S' & f' & I \\ f & S & 1 \end{Bmatrix} \times \begin{pmatrix} F' & 1 & F \\ -M'_F & 0 & M_F \end{pmatrix} \delta_{\ell'\ell}\delta_{I'I}\delta_{S'S}\delta_{S1}, \quad (21)$$

where $Q = F'+F+f'+f+I+\ell+S'-M'_F$ and the $\sqrt{6}$ arises from the reduced matrix element $\langle S||\hat{S}||S\rangle$ for $S = 1$. We

TABLE VI: Representative magnetic dipole transitions between a and X state levels with $\ell = 4$, driven by a linearly polarized MW magnetic field along z. Results for $a(v=38) \leftrightarrow X(v=139)$ and also for $a(v=37) \leftrightarrow X(v=138)$ are given. The top 3 lines specify the M_F values and the X state quantum numbers F_X and f_X, which are the same for both values of M_F. $F_X, f_X, E_X, g_{F_X}/F_a, f_a, E_a, g_{F_a}$ refer to levels that are primarily $X^1\Sigma_g^+/a^3\Sigma_u^+$. Energies ($E_X$ or E_a) (in GHz) are relative to the anchor level, $(f,\ell)F = (8{,}0)8$, which is at $E_b = -441.55$ GHz for $a(v=38)$ and at -515.14 GHz for $a(v=37)$. $\%X$ ($\%a$) gives the percent X (a) character. In each column, data on the most intense transition from the X level to a mostly a state level are given. The transition amplitude M_{M1} from Eq. 20 is given in units of μ_B. ΔE is the MW transition frequency in GHz. ΔW (in cm^{-1}) is the difference of the energy sensitivity of W to μ, for the two states of the transition, where $W = \mu\partial E/\partial\mu$ is the absolute change of E with respect to a fractional change $\Delta\mu/\mu$ in μ (see Ref. 1).

M_F	10	0	9	0	8	0
F_X	10	10	9	9	8	8
f_X	6	6	6	6	6	6
$a(v=38) \leftrightarrow X(v=139)$						
E_X	2.67		2.70		2.72	
$\%X$	72		71		74	
g_{F_X}	0.07		0.08		0.08	
F_a	10	9	9	8	8	9
f_a	6	5	6	5	6	6
E_a	-1.78	-7.38	-1.71	-7.54	-1.69	-1.71
$\%a$	73	100	73	100	72	73
g_{F_a}	0.20	0.06	0.19	0.06	0.22	0.19
M_{M1}	0.45	0.17	-0.21	0.17	-0.16	-0.05
ΔE	4.44	10.04	4.41	10.24	4.40	4.43
ΔW	65.	101.	63.	101.	64.	102.
$a(v=37) \leftrightarrow X(v=138)$						
E_X	-9.81		-9.80		-9.80	
$\%X$	89		89		89	
g_{F_X}	-5×10^{-3}		-7×10^{-3}		-6×10^{-3}	
F_a	10	9	9	10	8	9
f_a	6	5	6	7	6	7
E_a	-15.86	-7.24	-15.80	-7.45	-15.77	-7.51
$\%a$	94	78	93	99	93	99
g_{F_a}	-0.23	0.03	-0.24	0.04	-0.24	0.05
M_{M1}	0.11	-0.06	0.11	-0.09	-0.10	0.09
ΔE	6.05	-2.57	6.00	-2.36	5.97	-2.29
ΔW	132.	127.	132.	130.	137.	112.

note that, due to the $3j$ symbol in Eq. (21), $M_F = M'_F$ is required; moreover, when $F' = F$ the matrix element vanishes for $M_F = 0$ and increases monotonically with $|M_F|$. Conversely, when $F' = F \pm 1$ the matrix element decreases monotonically with $|M_F|$. Values of M_{M1} for a few specific transitions of interest are given in Table VI. Note that the transition amplitudes for $a(v = 37) \leftrightarrow X(v = 138)$ are systematically smaller than for $a(v = 38) \leftrightarrow X(v = 130)$; this is because the outer turning points for the X and a state potentials diverge (and hence Franck-Condon overlaps diminish) for the more deeply bound levels.

The last row for each set of the $a(v) \leftrightarrow X(v')$ transitions in Table VI gives the sensitivity of the transition to variations of the reduced mass, μ. This is labeled ΔW here, and corresponds to differences in $\partial_\mu E_\nu$ in Ref. [1]. It can be noted that in this regime, the more deeply bound level is more sensitive to variations of μ.

The data in Table VI provide transition frequencies and amplitudes as well as first-order magnetic sensitivities for a representative subset of possible MW transitions in Cs_2 that are sensitive to possible variations in μ. There are several examples of transitions with transition amplitude $M_{M1} \approx 0.2\ \mu_B$, such that a MW magnetic field with amplitude of 3 mG (corresponding to the same MW power needed for a 1 V/cm MW electric field, used earlier as a benchmark for E1 transitions) would drive transitions at a rate of $\approx 3 \times 10^3$/s. As for the E1 transitions, this should be adequately large for use in measuring energy splittings. These transitions have convenient MW frequencies, in the bands used for atomic clocks based on Cs (9.2 GHz) or H (1.4 GHz).

Magnetically insensitive ($M_F = M'_F = 0$) transitions are available if such states can be populated; we include g-factor data to allow estimates of the size of static B-field required to resolve Zeeman sublevels in such experiments, as well as of transition Zeeman shifts for other types of transitions should these be needed. Magnetic g_F factors are calculated from the diagonal matrix elements of S_z, in a manner analogous to that used for the $M1$ transition moments. Note that the difference in fractional X-state character between the states is roughly proportional to the sensitivity of that transition to μ; but for all transitions considered, that difference is of order unity.

VII. SUMMARY AND CONCLUSION

In summary, we have reported experimental data on the energies of several moderately bound states associated with the $a^3\Sigma_u^+$ potential of Cs_2. Using these data, together with most other available information on the a and $X^1\Sigma_g^+$ states, we have constructed a detailed model of the energy levels in these coupled ground-state potentials. The model reproduced and corroborated one case of significant singlet-triplet mixing between near-degenerate levels of the $X^1\Sigma_g^+$ and $a^3\Sigma_u^+$ states. This observation helps to locate the potentials of these two states relative to each other. Having said this, we also want to point out shortcomings of this work and opportunities for further progress on these states of Cs_2. Namely, (a) some of the residuals in the fit to the data are significantly larger than the estimated experimental errors; (b) data obtained elsewhere [18] closer to the dissociation limit, as well as Feshbach resonance data [13–15] were not included in the fit; and (c) in contrast with the recent work on analogous states of Rb_2 [10] that used a different pathway for spectroscopy, the experimental information on hyperfine structure and H_{SO2} interactions extended only modestly below the dissociation limit.

Nevertheless, in view of its (limited) success, we have used our model to calculate $E1$ and $M1$ transition matrix elements between nearly-degenerate pairs of levels, whose splitting is sensitive to possible variations in the fundamental constant μ. Based on the calculated values of the splittings and the transition moments, we have suggested several specific pairs of levels that appear suitable for experiments seeking evidence for variation in μ, of the type proposed in Ref. [1]. These calculations should be useful as a guide for designing new experiments of this type, and more generally in understanding the structure of the Cs_2 molecule.

More generally, we reiterate the concluions of [1], namely: it appears feasible to construct an atomic fountain-type experiment based on Cs_2 to search for varations of μ with unprecedented sensitivity. As argued in Ref. [1], an experiment of this type using carefully chosen molecular transitions in Cs_2 (such as those discussed here) could conceivably be used to search for fractional variations in μ at the level of ≈ 1 part in 10^{17}/year. We note as well that it was recently pointed out [59] that the same molecular transitions are also highly sensitive to possible variations in the fine structure constant α. The discussion of this paper has been couched in terms of a search for variation in μ, but is equally applicable to both cases.

Acknowledgments We thank Nadia Bouloufa and Olivier Dulieu for sending us their latest 0_g^- potential. Work at Temple University was supported from NSF grant PHY-1005453 and from an AFOSR MURI. Work at Stony Brook was supported by the US NSF under grants PHY0652459 and PHY0968905. Also, at an early stage, TB benefited from allocations at the National Center for Supercomputing Applications (NCSA, at the University of Illinois) under awards PHY070038N and PHY100021. The work at Yale was supported by DOE, NSF, and AFOSR-MURI.

[1] D. DeMille, S. Sainis, J. Sage, T. Bergeman, S. Kotochigova, and E. Tiesinga, Phys. Rev. Lett. **100**, 043202 (2008).

[2] T. Zelevinsky, S. Kotochigova and J. Ye, Phys. Rev. Lett. **100**, 043201 (2008).

[3] S. Sainis, Ph. D. Thesis, Yale University (2006) (unpublished).

[4] C. Samuelis, E. Tiesinga, T. Laue, M. Elbs, H. Knöckel, and E. Tiemann, Phys. Rev. A **63**, 012710 (2000).

[5] L. E. E. de Araujo, J. D. Weinstein, S. D. Gensemer, F. K. Fatemi, K. M. Jones, P. D. Lett and E. Tiesinga, J. Chem. Phys., **119**, 2062 (2003).

[6] A. Pashov, O. Docenko, M. Tamanis, R. Ferber, H. Knöckel and E. Tiemann, Phys. Rev. A **72**, 062505 (2005).

[7] O. Docenko, J. Zaharova, M. Tamanis, R. Ferber, A. Pashov, H. Knöckel and E. Tiemann, J. Phys. B 39, S929 (2006).

[8] P. Staanum, A. Pashov, H. Knöckel, and E. Tiemann, Phys. Rev. A **75**, 042513 (2007).

[9] A. Pashov, O. Docenko, M. Tamanis, R. Ferber, H. Knöckel, and E. Tiemann, Phys. Rev. A **76**, 022511 (2007).

[10] C. Strauss, T. Takekoshi, F. Lang, K. Winkler, R. Grimm, J. HeckerDenschlag and E. Tiemann, Phys. Rev. A **82**, 052514 (2010).

[11] D. Li, F. Xie, L. Li, S. Magnier, V. Sovkov and V. Ivanov, Chemical Physics Letters, **441**, 39 (2007).

[12] F. Xie, V. Sovkov, A. M. Lyyra, D. Li, S. Ingram, J. Bai, V. Ivanov, S. Magnier and L. Li, J. Chem. Phys. **130**, 051102 (2009).

[13] V. Vuletić, A. J. Kerman, C. Chin and S. Chu, Phys. Rev. Lett. **82**, 1406 (1999).

[14] C. Chin, V. Vuletić, A. J. Kerman and S. Chu, Phys. Rev. Lett. **85**, 2717 (2000).

[15] M. Mark, F. Ferlaino, S. Knoop, J. G. Danzl, T. Kraemer, C. Chin, H.-C. Nägerl and R. Grimm, Phys. Rev. A **76**, 042514 (2007).

[16] P. J. Leo, C. J. Williams and P. S. Julienne, Phys. Rev. Lett., **85**, 2721 (2000).

[17] C. Chin, V. Vuletić, A. J. Kerman, S. Chu, E. Tiesinga, P. J. Leo and C. J. Williams, Phys. Rev. A **70**, 032701 (2004).

[18] N. Vanhaecke, C. Lisdat, B. T'Jampens, D. Comparat, A. Crubellier and P. Pillet, Eur. Phys. J. D **28**, 351 (2004).

[19] C. Amiot and O. Dulieu, J. Chem. Phys. **117**, 5155 (2002).

[20] (a)R. Rydberg, Z. Phys. **73**, 376 (1931); (b) O. Klein, *ibid.*, **76**, 226 (1932); (c) R. Rydberg *ibid.*, **80**, 514 (1933); (d) A. L. G. Rees, Prof. Phys. Soc. London **59**, 998 (1947).

[21] C. R. Vidal and H. Scheingraber, J. Mol. Spectrosc. **65**, 46 (1977).

[22] H. Weickenmeier, U. Diemer. Demtröder and M. Broyer, Chem. Phys. Lett. **124**, 470 (1986).

[23] J.G. Danzl, E. Haller, M. Gustavsson, M. J. Mark, R. Hart, N. Bouloufa, O. Dullieu, H. Ritsch and H.-C. Nägerl, Science **321**, 1062 (2008)

[24] J. A. Coxon and P. G. Hajigeorgiou, J. Chem. Phys. **132**, 094105 (2010).

[25] R. S. Freund, T. A. Miller, D. De Santis and A. Lurio, J. Chem. Phys. **53**, 2290 (1970).

[26] D. De Santis, A. Lurio, R. S. Freund and T. A. Miller, J. Chem. Phys. **58**, 4625 (1970).

[27] E. R. I. Abraham. W. I. McAlexander, C. A. Sackett and R. G. Hulet, Phys. Rev. Lett. **74**, 1315 (1995).

[28] A. Fioretti, D. Comparat, C. Drag, T. F. Gallagher and P. Pillet, Phys. Rev. Lett., **82**, 1839 (1999)

[29] C. Drag, B. Laburthe Tolra, O. Dulieu, D. Comparat, M. Vatasescu, S. Boussen, S. Guibal, A. Crubellier and P. Pillet, IEEE J. Quan. Electron. **36**, 1378 (2000).

[30] M. Vatasescu, O. Dulieu, C. Amiot, D. Comparat, C. Drag, V. Kokoouline, F. Masnou-Seeuws, and P. Pillet, Phys. Rev. A **61**, 044701 (2000); M. Vatasescu, C. Dion and O. Dulieu, J. Phys. B **39**. S945 (2006).

[31] W. Ketterle, K. B. Davis, M. A. Joffe, A. Martin, and D. E. Pritchard, Phys. Rev. Lett. **70**, 2253 (1993).

[32] M. H. Anderson, W. Petrich, J. R. Ensher, and E. A. Cornell, Phys. Rev. A **50**, R3597 (1994).

[33] A. Fioretti, D. Comparat, A. Crubellier, O. Dulieu, F. Masnou-Seeuws and P. Pillet, Phys. Rev. Lett. **80**, 4402 (1998).

[34] B. Laburthe Tolra, C. Drag and P. Pillet, Phys. Rev. A **64**, 061401 (2001).

[35] C. Lisdat, N. Vanhaecke, D. Comparat and P. Pillet, Eur. Phys. J. D **21**, 299 (2002).

[36] D. Comparat, C. Drag, B. Laburthe Tolra, A. Fioretti, P. Pillet, A. Crubellier, O. Dulieu and F. Masnou-Seeuws, Eur. Phys. J. D **11**, 59 (2000).

[37] N. Bouloufa, A. Crubellier, and O. Dulieu, Phys. Rev. A **75**, 052501 (2007).

[38] Supplementary data file.

[39] E. Arimondo, M. Inguscio and P. Violino, Rev. Mod. Phys. **49**, 31 (1977).

[40] S. Kotochigova, E. Tiesinga and P. S. Julienne, Phys. Rev. A **63**, 012517 (2000).

[41] K. M. Jones *et al.*, Europhys. Lett. **35**, 85 (1996).

[42] R. J. Le Roy, Can. J. Phys. **52**, 246 (1974).

[43] O. Docenko, M. Tamanis, R. Ferber, A. Pashov, H. Knöckel, and E. Tiemann, Eur. Phys. J. D **31**, 205 (2004).

[44] R. J. Le Roy and R. D,. E. Henderson, Mol. Phys. **105**, 663 (2007).

[45] D. Colbert and W. H. Miller, J. Chem. Phys. **96**, 1982 (1992).

[46] E. Tiesinga, C. J. Williams and P. S. Julienne, Phys. Rev. A **57**, 4257 (1998).

[47] R. A. Frosch and H. M. Foley, Phys. Rev. A **88**, 1337 (1952).

[48] J. M. Brown and A. Carrington, "Rotational Spectroscopy of Diatomic Molecules", Cambridge U. Press", Cambridge, U.K., 2003.

[49] R. W. Field and H. Lefebvre-Brion. *The Spectra and Dynamics of Diatomic Molecules*, Elsevier, Amsterdam, 2004.

[50] M. Krauss and W. J. Stevens, J. Chem. Phys. **93**, 4236 (1990).

[51] M. Aubert-Frécon, private communication (2005-6).

[52] M. Foucrault, Ph. Millie, and J. P. Daudey, J. Chem. Phys. **96**, 1257 (1992).

[53] M. Marinescu and A. Dalgarno, Phys. Rev. A. **52**, 311 (1995).

[54] A. Derevianko, W. R. Johnson, M. S. Safronova and J. F. Babb, Phys. Rev. Lett., **82**, 3589 (1999).

[55] J. G. Danzl, M. J. Mark. E. Haller, M. Gustavsson, R. Hart, J. Aldegunde, J. M. Hutson, H.-C. Nägerl, Nature Physics **6**, 265 (2010).

[56] P. A. Malmqvist, A. Rendell, and B. Roos, J. Phys. Chem. **94**, 5477 (1990).

[57] O. Docenko, M. Tamanis, R. Ferber, T. Bergeman, S. Kotochigova, A. V. Stolyarov, A. de Faria Nogueira, and

C. E. Fellows, Phys. Rev. A **81**, 042511 (2010).
[58] F. Mies, C. J. Williams, P. S. Julienne, and M. Krauss, J. Res. Natl. Inst. Stand. Technol. **101**, 521 (1996).
[59] K. Beloy, A. Borschevsky, V.V. Flambaum, and P. Schwerdtfeger, Phys. Rev. A **84**, 042117 (2011).
[60] J. G. Danzl, M. J. Mark. E. Haller, M. Gustavsson, R. Hart,